Quasi-one-dimensional sliding ferroelectricity in NbI_4

Ning Ding, Haoshen Ye, and Shuai Dong *

Key Laboratory of Quantum Materials and Devices of Ministry of Education, School of Physics, Southeast University, Nanjing 21189, China

(Received 15 May 2024; revised 17 June 2024; accepted 16 July 2024; published 31 July 2024)

Sliding ferroelectricity was originally proposed to elucidate the out-of-plane polarization generated by a specific stacking arrangement of nonpolar van der Waals layers. However, the concept of sliding ferroelectricity can be generalized to more geometries. Here, the NbI_4 bulk is theoretically demonstrated as a quasi-one-dimensional sliding ferroelectric material, which exhibits a polarization of 0.11 $\mu C/cm^2$ perpendicular to the Nb's chains. The most possible ferroelectric switching path is found to be via the interchain sliding along the chain direction, while other paths such as Peierls dimerization of Nb pairs may also work. Moreover, its polarization can be augmented for 82% by hydrostatic pressure up to 10 GPa, beyond which NbI_4 becomes a polar metal. In addition, negative longitudinal piezoelectricity is also predicted.

DOI: 10.1103/PhysRevB.110.024115

I. INTRODUCTION

In recent years, low-dimensional ferroelectrics has emerged as a promising branch of polar materials, which may overcome the critical size effect to maintain stable ferroelectric polarization in the atomic limit [1–5]. Among two-dimensional (2D) ferroelectrics, there are several extensively studied subbranches including $CuInP_2S_6$ [6], α-In_2Se_3 [7], SnTe [8], $NbOI_2$ [9], and WO_2Cl_2 [10]. All of them belong to ion displacement type ferroelectrics.

Interlayer sliding ferroelectricity, proposed by Wu *et al.* [11], widely exists in 2D van der Waals (vdW) materials. Their out-of-plane ferroelectric polarizations are induced by specific stacking modes, which can be reversed by interlayer sliding [12]. Until now, the experimentally confirmed sliding ferroelectrics include WTe_2 bilayer/few-layer/flakes [13–15], hexagonal BN bilayer [16,17], *R*-MX_2 (M = Mo/W, X = S/Se) [18], $1T'$-ReS_2 bilayer [19], and InSe bilayer [20]. In addition to these binary-element compounds, sliding ferroelectricity was also reported in the inorganic-organic hybrid vdW crystal (15-crown-5)Cd_3Cl_6 [21]. In addition, a large number of sliding ferroelectrics have been theoretically predicted [22–32]. Furthermore, a general theory for bilayer stacking ferroelectricity was also established based on a group theory analysis [33], which can provide the design rule for sliding ferroelectric bilayers.

The ferroelectricity in quasi-one-dimensional systems has also received lots of attention, such as poly(vinylidene fluoride-trifluoroethylene) (P(VDF-TrFE)) nanowire [34], group-IV metal chalcogenides nanowires and nanotubes [35,36], SbN/BiN nanowires [37], and vdW oxyhalides WOX_4 and $NbOX_3$ (X = Cl, Br, I) [38–40]. Because of the quasi-one-dimensional characteristics, the theoretical upper limit for ferroelectric memory density can reach ~100 Tbits/in.^{2} [38]. Therefore, it will be interesting to generalize the concept of sliding ferroelectricity into quasi-one-dimensional systems, because sliding ferroelectricity is naturally superior to other nonsliding ferroelectrics regarding the switching energy [41]. However, sliding ferroelectricity has not been touched in quasi-one-dimensional systems.

In this paper, the quasi-one-dimensional NbI_4 vdW bulk with $4d^1$ electron configuration will be theoretically studied. The two chains within one primitive cell can slide, which leads to a dipole perpendicular to the chain direction. Nontrivially, this interchain sliding is driving by intrachain Peierls dimerization. Multiple ferroelectric switching paths are allowed to reverse polarization. Furthermore, its sliding polarization can be enhanced by 82% under 10 GPa hydrostatic pressure, beyond which it becomes a polar metal. The intriguing negative longitudinal piezoelectric effect is also revealed in this vdW material.

II. METHODS

First-principles calculations were performed with the projector augmented-wave (PAW) potentials as implemented in the Vienna *ab initio* simulation package (VASP) [42]. The Perdew-Burke-Ernzerhof (PBE) parametrization of the generalized gradient approximation (GGA) was used for the exchange-correlation functional [43]. The plane-wave cutoff energy was 500 eV, and the Nb's $5s4d4p4s$ electrons were treated as valence states. The k-point grid of $5 \times 5 \times 3$ was employed for structural relaxation and static computation. To describe the interchain interaction, two different types of vdW corrections of dispersion-corrected density functional theory DFT-D2 and DFT-D3 were used for comparison [44,45]. The convergence criterion of energy was set to 10^{-6} eV, and the criterion of Hellman-Feynman forces during the structural relaxation was 0.005 eV/Å.

The phonon spectrum calculation was used by the finite-difference method [46,47]. The polarization was calculated by the standard Berry phase method [48,49]. In order to describe the correlated d electrons, the Hubbard U_{eff} with the Dudarev

*Contact author: sdong@seu.edu.cn

TABLE I. The lattice constants of the NbI_4 bulk from DFT calculations and experiment (Expt.), which are in units of Å. $\alpha/\beta/\gamma$ indicate the crystallographic axis angles, in units of degrees. D2 and D3 indicate different vdW corrections in DFT calculations. The original experimental data are for orthorhombic axes ($a = a'$, $b = \sqrt{3}b'$, $c = c'$). It is clear the DFT-D2 calculation leads to the best description of the structure.

	a'	b'	c'	α	β	γ
GGA	8.159	8.159	15.265	90	90	122.90
GGA+D2	7.648	7.648	13.927	90	90	118.98
GGA+D3	7.721	7.721	14.196	90	90	119.71
Expt. [53]	7.646	7.646	13.930	90	90	119.79

approximation was applied [50]. In addition, the linear response ansatz was used to estimate the appropriate U_{eff} [51].

III. RESULTS AND DISCUSSION

A. Crystalline and electronic structures

Figures 1(a) and 1(b) show the structures of the NbI_4 bulk in the primitive cell with the space group $Cmc2_1$ (No. 36). The transformation matrix between the conventional (original experimental) cell [labeled as (a, b, c)] and the primitive cell [labeled as (a', b', c')] with the space group $Cmc2_1$ is $(a, b, c)^T = \begin{pmatrix} 1 & 1 & 0 \\ -1 & 1 & 0 \\ 0 & 0 & 1 \end{pmatrix}(a', b', c')^T$, as depicted in Fig. S1 [52]. The lattice constants optimized by the DFT+D2 vdW correction with pure GGA are $a' = b' = 7.648$ Å and $c' = 13.927$ Å, which agree best with the experimental values $a' = b' = 7.646$ Å and $c' = 13.930$ Å [53], as compared in Table I. Thus, in the following calculation, the D2 correction will be used by default. In the primitive cell, there are two NbI_4 chains, and these two chains are assembled by vdW force.

Within each chain, every Nb ion is caged within the I_6 octahedron and the neighbor octahedra are edge sharing. Interestingly, two adjacent Nb ions are dimerized, with a significant disproportion of nearest-neighbor Nb-Nb distances: the longer one $d_l = 4.450$ Å and the shorter one $d_s = 3.316$ Å as depicted in Fig. 1(b). The phonon spectrum is calculated as shown in Fig. 1(c), and there are no imaginary frequencies in the whole Brillouin zone, implying its dynamic stability.

The calculated electronic structure indicates that NbI_4 is a semiconductor with an indirect band gap 0.41 eV, as shown in Fig. 1(d). The top valence bands are dominated by the I's $5p$ and Nb's $4d_{xy}$ orbitals. For shorter Nb-Nb pairs, the overlap between two $4d^1$ electron orbitals is stronger, forming the bonding state (i.e., the σ bond). The partial charge density for the top valence bands (within $[-0.5, 0]$ eV) is calculated, which indicates the forming of a molecular orbital between the shorter Nb-Nb pairs, as shown in Fig. 1(b). The electronic band structure of NbI_4 without Nb-Nb dimerization is shown in Fig. S2 [52], which indicates a metallic electronic structure. In this sense, the structural dimerization is a kind of Peierls transition driving the half-filling electron density. This molecular orbital, i.e., the bonding state, is occupied by two electrons of Nb-Nb pairs, leading to a zero net magnetic moment. Since its point group ($mm2$) is polar, a polarization is estimated as 0.13 $\mu C/cm^2$, along the c axis.

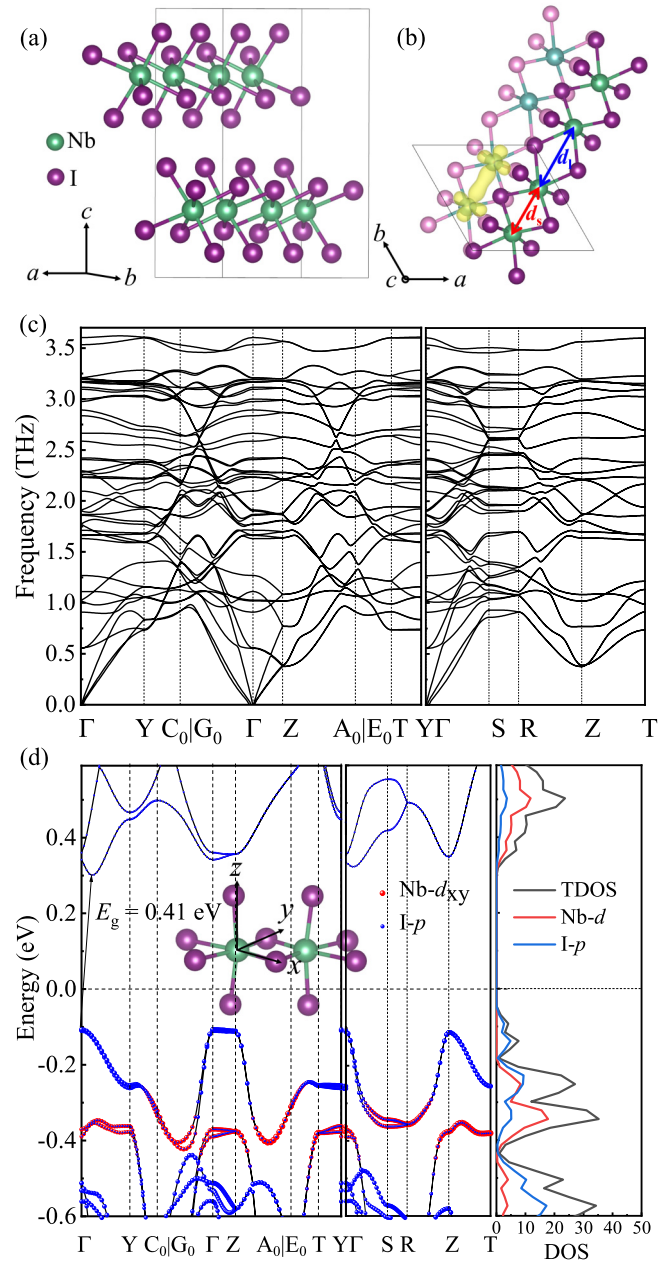

FIG. 1. (a) Side view of NbI_4 bulk. Each unit cell (u.c.) contains two chains coupled by vdW force. (b) View of NbI_4 bulk from the c axis. The structural dimerization of Nb ions can be indicated by the longer d_l and shorter d_s. Correspondingly, the electron occupancy forms a molecular orbital between the shorter Nb-Nb pair, as indicated by the yellow shadow. (c) The phonon spectrum. (d) The electronic band structure and corresponding density of states (DOS). The red and blue curves indicate the contributions from Nb's d and I's p orbital, respectively. Inset: Cartesian coordinates used for orbital decomposition.

To account for the possible Hubbard correction, the spin-polarized GGA+U calculation is also performed. The physical properties such as lattice constants, band gaps, and polarization are calculated as a function of U_{eff}.

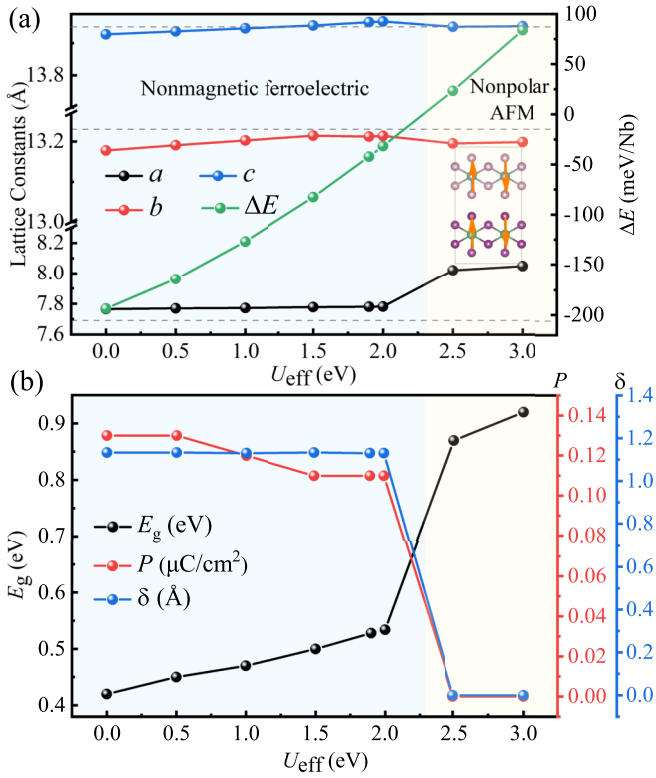

FIG. 2. (a) The lattice constants and energy difference (ΔE) between the polar nonmagnetic (NM) state and nonpolar antiferromagnetic (AFM) state as a function of U_{eff}. Inset: The magnetic order, which is Néel-type antiferromagnetic within each chain but ferromagnetically coupled between chains. However, the interchain exchange is much weaker than the intrachain one. Note the basis vectors are uniformed to be the orthogonal ones (a, b, c). Here, the lattice constant along the b axis is doubled for the nonpolar antiferromagnetic state (*Pbam*). (b) Physical properties as a function of U_{eff}, including the band gap (E_g), polarization (P), and intensity of Peierls distortion ($\delta = d_l - d_s$).

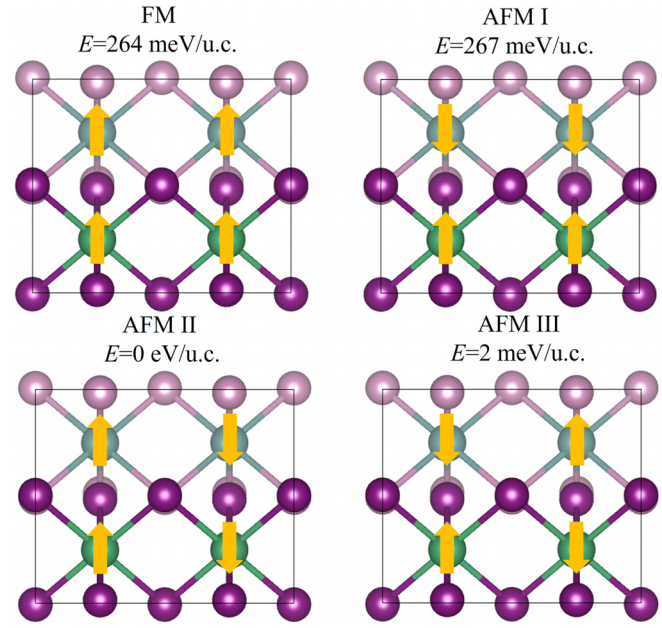

FIG. 3. Possible magnetic orders and corresponding DFT energies. The antiferromagnetic (AFM) II is the ground state, with Néel antiferromagnetic order in the chain but FM coupling between chains.

Considering the d^1 fact, a simple Néel antiferromagnetic state [inset of Fig. 2(a)] is also calculated for comparison. As shown in Fig. 2(a), the nonmagnetic state is more energetically favorable, and its lattice constants are almost unaffected with increasing U_{eff} when $U_{\text{eff}} \leqslant 2$ eV. Since the Hubbard interaction tends to cause a Mott transition, namely to split the spin-up and spin-down channels to form local magnetic moments and a large Mott band gap, here, the Mott transition occurs once $U_{\text{eff}} \geqslant 2.5$ eV, so the magnetic state becomes more stable, with the lattice constant a expanding (∼3%) as a result of the disappearance of the Peierls transition. Accompanying this nonmagnetic-magnetic transition, a structural transition to *Pbam* (No. 55) occurs and the Peierls transition disappears, leading to the dissolution of the molecular orbital. As a result, the local magnetic moment $\sim 1\mu_B$/Nb appears, as expected for the $4d^1$ configuration. Consequently, the system changes from a band insulator to a Mott insulator with a larger band gap, as shown in Fig. 2(b). Since the point group of the magnetic state (*mmm*) is nonpolar, the polarization also disappears. Four possible magnetic orders are considered, with ferromagnetic/antiferromagnetic orders within/between chains as depicted in Fig. 3. The DFT energies indicate that the Néel antiferromagnetic order is stable in each chain, while the interchain coupling is weakly ferromagnetic (AFM II). Its phonon spectrum is also dynamically stable, as shown in Fig. S3 [52]. In addition, the spin-orbital coupling (SOC) effect is also taken into consideration to double check the physical properties as depicted in Fig. S4 [52].

In short, the NbI_4 bulk can be nonmagnetic ferroelectric or nonpolar antiferromagnetic, depending on the Hubbard U_{eff}. This behavior seems to be similar to the recently proposed idea of "alterferroicity" [54], if its real Hubbard U_{eff} can be tuned across the phase transition boundary. To test this idea, the effective Hubbard parameter U_{eff} is estimated using the linear response ansatz method [51], which leads to 1.9 eV. Therefore, the ground state of the NbI_4 bulk should stay in the nonmagnetic ferroelectric side but indeed be close to the transition boundary. The DFT results at $U_{\text{eff}} = 1.9$ eV agree well with the experimental structure: a polar structure and very precise lattice constants (the error bar is less than 1%). Therefore, all the following calculations are performed with $U_{\text{eff}} = 1.9$ eV.

B. Sliding ferroelectricity

As aforementioned, the space group of NbI_4 bulk calculated by GGA+D2+U ($U_{\text{eff}} = 1.9$ eV) is $Cmc2_1$ (No. 36), which belongs to the polar point group *mm*2. Using the standard Berry phase calculation, the polarization is estimated as 0.11 μC/cm^2, pointing along the c axis, which is comparable to other typical sliding ferroelectrics, e.g., 0.03 μC/cm^2 in WTe_2 bilayer and 0.68 μC/cm^2 in h-BN bilayer [11,55,56].

Although each chain of NbI_4 is nonpolar, the specific binding mode of chains results in the polar structure, i.e., the interchain sliding. According to the empirical rule in

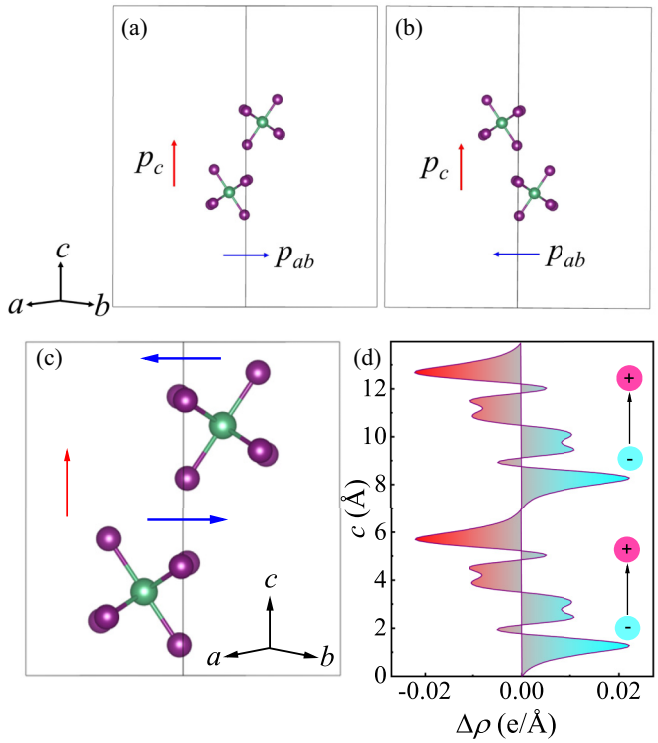

FIG. 4. Origin of interchain sliding ferroelectricity in NbI_4 bulk. (a), (b) Two isolated two chains with different binding modes: (a) A-B binding vs (b) B-A binding. (c) Top view of chains in bulk. The induced dipoles are perpendicular to the chains. However, its component in the *ab* plane (blue) is canceled in the bulk, while only the component along the *c* axis (red) gives an increase to the net polarization. (d) The planar-averaged differential electron density $\Delta\rho$ between the $+P$ and $-P$ states along the *c* axis. The *c* positions in (c) and (d) are in a one-to-one correspondence.

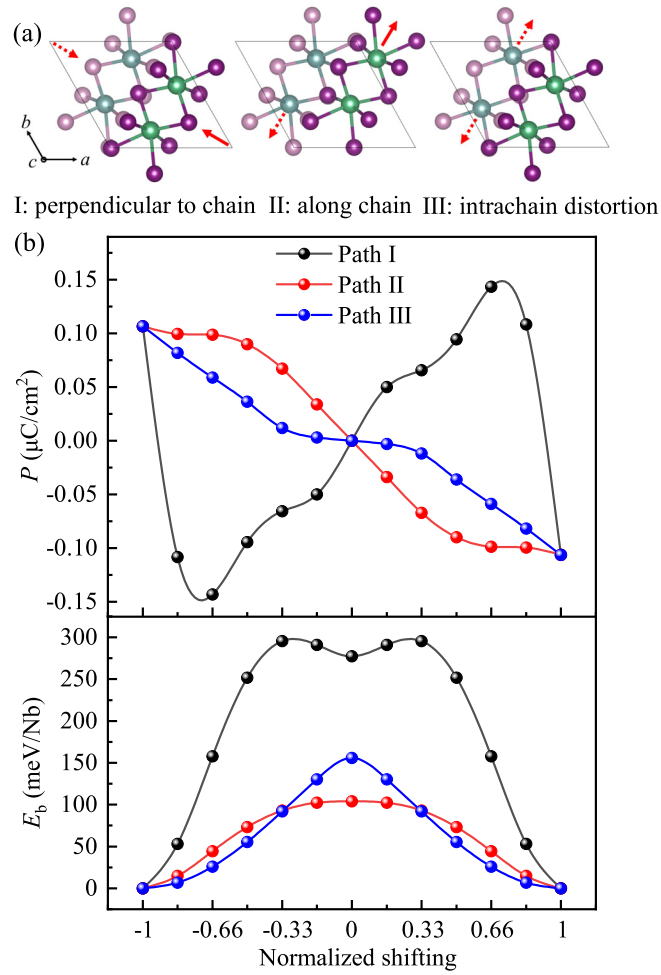

FIG. 5. (a) Three possible switching paths of polarization (*P*) in NbI_4 bulk. (b) Corresponding polarizations and energy barriers for these three switching paths. Horizontal axis: The interchain sliding and intrachain distortion are normalized.

2D sliding ferroelectrics, the induced polarization should be perpendicular to the sliding direction, i.e., along the out-of-plane axis. However, for quasi-one-dimensional chains, the sliding is along the chain direction, and thus there are two perpendicular directions. As depicted in Figs. 4(a) and 4(b), our calculation on two isolated chains indeed finds two perpendicular components (p_c and p_{ab}) of dipoles for each pair of chains. For two isolated chains, the calculated dipole along (a, b, c) is (-0.0044, 0.0044, -0.0682) e Å for the A-B binding mode, but (0.0044, -0.0044, -0.0682) e Å for the B-A binding mode. Interestingly, the p_c's are parallel between nearest-neighbor pairs. In contrast, p_{ab}'s are antiparallel and canceled between nearest-neighbor pairs along the *c* axis. As summarized in Fig. 4(c), the induced polarization is only along the *c* axis in its vdW bulk.

To trace the microscopic origin of dipoles, the planar-averaged differential electron density is calculated along the *c* axis, defined as $\Delta\rho = \iint[\rho(+P) - \rho(-P)]dxdy$ between opposite polarization states. As shown in Fig. 4(d), the bias of the electron cloud can be unambiguously visualized. As expected, the neighboring I ions between chains contribute most to the induced dipole.

The quasi-one-dimensional characteristic of NbI_4 provides more degrees of freedom regarding its sliding modes. Specifically, the slidings along the direction of the chain and perpendicular to the chain are shown in Fig. 5(a), which can reverse polarization. In addition, the polarization can also be reversed via intrachain ion displacements, namely by altering the phase of Peierls dimerization in half of the chains. These three ferroelectric switching paths (labeled as I, II, and III) are investigated via linear interpolation.

As shown in Fig. 5(b), the polarizations and energy barriers of these three paths as a function of normalized shift are quite different. Path I, with rigid interchain sliding perpendicular to the chains, has the highest-energy barrier ~295 meV/f.u. Correspondingly, the change of polarization is not monotonic, but in an exotic trajectory. Path II, with rigid interchain sliding along the chain direction, has the lowest-energy barrier ~100 meV/f.u. Path III, by changing the phase of Peierls dimerization in one chain, has a middle energy barrier ~156 meV/u.c. For both paths II and III, the polarization changes normally as a function of normalized shifting: It decreases to zero first and then increases in the opposite direction. With the lowest-energy barrier, path II may be the most possible one in a real switching process. In fact, the theoretical paths are all presumptive, but other possible switching modes (including those hybrid ones) cannot be excluded in real cases.

C. Negative piezoelectricity and polar metal

Piezoelectricity is an important physical property of ferroelectric materials. In vdW ferroelectrics, negative piezoelectricity often appears as an inborn characteristic of low-dimensional materials [57,58]. However, previous studies on negative piezoelectricity were mostly focused on 2D materials and the investigation of piezoelectricity in quasi-one-dimensional sliding ferroelectrics is lacking. This work helps to fill the gap.

In order to investigate the piezoelectric property of NbI_4 bulk, the elastic matrix and the piezoelectric tensor matrix are calculated by the energy-strain method and density functional perturbation theory (DFPT) method [59,60], respectively. There are nine independent nonzero matrix elements for the space group $Cmc2_1$ in an elastic matrix (in units of GPa) [61]:

$$C=\begin{pmatrix} 73.404 & 13.015 & 11.936 & 0 & 0 & 0 \\ 13.015 & 42.489 & 8.819 & 0 & 0 & 0 \\ 11.936 & 8.819 & 45.130 & 0 & 0 & 0 \\ 0 & 0 & 0 & 9.354 & 0 & 0 \\ 0 & 0 & 0 & 0 & 12.062 & 0 \\ 0 & 0 & 0 & 0 & 0 & 13.768 \end{pmatrix}. \quad (1)$$

The piezoelectric tensor matrix has five independent nonzero matrix elements in units of C/m^2 for point group $mm2$ [62]:

$$e=\begin{pmatrix} 0 & 0 & 0 & 0 & -8.61 & 0 \\ 0 & 0 & 0 & -0.77 & 0 & 0 \\ 6.24 & 3.59 & -16.25 & 0 & 0 & 0 \end{pmatrix}. \quad (2)$$

Then the piezoelectric strain coefficient d_{ij} can be calculated as

$$d_{ij}=\sum_{k=1}^{6} e_{ik}C_{kj}^{-1}. \quad (3)$$

The piezoelectric strain coefficients d_{ij} in units of pC/N are

$$d=\begin{pmatrix} 0 & 0 & 0 & 0 & -0.63 & 0 \\ 0 & 0 & 0 & -0.06 & 0 & 0 \\ 0.13 & 0.13 & -0.42 & 0 & 0 & 0 \end{pmatrix}. \quad (4)$$

The calculated d_{33} is -0.42 pC/N, indicating a negative piezoelectricity in this quasi-one-dimensional sliding ferroelectric. It means that the polarization is enhanced when the lattice is shrinking along the polarization direction, or vice versa. The mechanism of the negative piezoelectricity of NbI_4 is similar to that of interlayer sliding ferroelectricity [25], which is the joint contribution of the increase in the dipole moment and a decrease in volume. In other words, the closer the neighboring NbI_4 chains, the larger is the interchain sliding and the stronger is the dipole moment within a smaller volume. Consequently, a larger polarization perpendicular to the chains is induced.

There are two competing phases (polar versus magnetic) in the NbI_4 bulk, whose volumes are different. Naturally, the pressure is an effective strategy to regulate phase transitions. Finally, the effect of hydrostatic pressure is investigated. The lattice constants and Peierls dimerization are depicted in Fig. 6(a) as a function of hydrostatic pressure. As expected, the lattice constants decrease significantly. For example, at 9 GPa, a, b, and c shrink for 5.1%, 8.3%, and 7.1%, respectively, and the volume is reduced for 19.2%. For comparison, the Peierls dimerization δ only decreases for 3.0%, due to the stiffness of the intrachain.

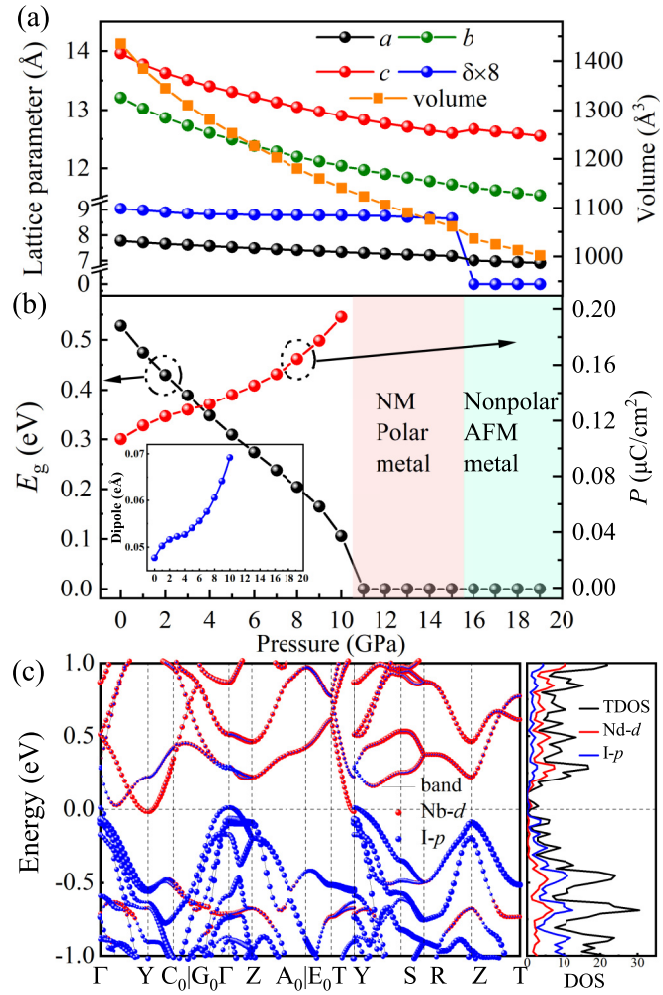

FIG. 6. (a) The lattice parameters including lattice constants and eight times Peierls dimerization (characterized by $\delta \times 8$) as a function of hydrostatic pressure. Note the basis vectors are uniformed to be the orthogonal ones (a, b, c). The unit cell of the $Cmc2_1$ one is doubled along the b axis compared with the $Pbam$ one. Thus, the corresponding lattice constant for the $Pbam$ phase is $2b$. (b) Band gap and polarization as a function of hydrostatic pressure. Inset: The dipole of one unit cell as a function of pressure in the ferroelectric region. (c) The electron band structure and density of states under a pressure of 11 GPa (i.e., in the polar metal region).

In consistent with the negative piezoelectricity, the polarization is promoted for 82% by hydrostatic pressure up to 10 GPa, as shown in Fig. 6(b). The physical origin is not only the reduction in volume but also the enhanced dipole [inset of Fig. 6(b)] of NbI_4 chains, which is also similar to the interlayer sliding ferroelectricity [25].

As expected, the band gap decreases with hydrostatic pressure, as shown in Fig. 6(b). Beyond 10 GPa, the band gap of NbI_4 bulk closes while its polar structure remains. In

other words, it becomes a polar metal. The typical electron band structure is shown in Fig. 6(c). Such a pressure-induced insulator-metal transition belongs to the Bloch-Wilson transition, which also widely exists in pressurized superconductors [63]. With further increasing pressure ($\geqslant$16 GPa), the Néel-type antiferromagnetic state appears with suppressed Peierls dimerization based on the enthalpy difference between nonmagnetic polar and nonpolar antiferromagnetic states (Fig. S5 [52]).

IV. CONCLUSION

In summary, based on first-principles calculations, the structural and electronic properties of NbI_4 vdW bulk have been studied systematically. The structural Peierls dimerization within its one-dimensional chain quenches the local magnetic moment of the $4d^1$ electron. Binding between two chains induces charge redistribution and further leads to polarization, which can be switched by the interchain sliding. In addition, the negative piezoelectricity effect is predicted. In addition, the polarization can be enlarged for 82% by hydrostatic pressures up to 10 GPa, beyond which NbI_4 becomes a polar metal. With further increasing pressure ($\geqslant$16 GPa), the Néel-type antiferromagnetic state appears with suppressed Peierls dimerization and polarization.

ACKNOWLEDGMENTS

This work supported by the National Natural Science Foundation of China (Grants No. 12274069 and No. 12325401) and Jiangsu Funding Program for Excellent Postdoctoral Talent under Grant No. 2024ZB001. We thank the Big Data Center of Southeast University for providing the facility support on the numerical calculations.

[1] C. Wang, L. You, D. Cobden, and J. Wang, Towards two-dimensional van der Waals ferroelectrics, Nat. Mater. **22**, 542 (2023).
[2] D. Zhang, P. Schoenherr, P. Sharma, and J. Seidel, Ferroelectric order in van der Waals layered materials, Nat. Rev. Mater. **8**, 25 (2023).
[3] M. Wu and P. Jena, The rise of two-dimensional van der Waals ferroelectrics, WIREs Comput. Mol. Sci. **8**, e1365 (2018).
[4] Z. Guan, H. Hu, X. Shen, P. Xiang, N. Zhong, J. Chu, and C. Duan, Recent progress in two-dimensional ferroelectric materials, Adv. Electron. Mater. **6**, 1900818 (2020).
[5] L. Qi, S. Ruan, and Y.-J. Zeng, Review on recent developments in 2D ferroelectrics: Theories and applications, Adv. Mater. **33**, 2005098 (2021).
[6] F. Liu, L. You, K. L. Seyler, X. Li, P. Yu, J. Lin, X. Wang, J. Zhou, H. Wang, H. He *et al.*, Room-temperature ferroelectricity in $CuInP_2S_6$ ultrathin flakes, Nat. Commun. **7**, 12357 (2016).
[7] W. Ding, J. Zhu, Z. Wang, Y. Gao, D. Xiao, Y. Gu, Z. Zhang, and W. Zhu, Prediction of intrinsic two-dimensional ferroelectrics in In_2Se_3 and other III_2-VI_3 van der Waals materials, Nat. Commun. **8**, 14956 (2017).
[8] K. Chang, J. Liu, H. Lin, N. Wang, K. Zhao, A. Zhang, F. Jin, Y. Zhong, X. Hu, W. Duan, Q. Zhang, L. Fu, Q.-K. Xue, X. Chen, and S.-H. Ji, Discovery of robust in-plane ferroelectricity in atomic-thick SnTe, Science **353**, 274 (2016).
[9] Y. Jia, M. Zhao, G. Gou, X. C. Zeng, and J. Li, Niobium oxide dihalides $NbOX_2$: A new family of two-dimensional van der Waals layered materials with intrinsic ferroelectricity and antiferroelectricity, Nanoscale Horiz. **4**, 1113 (2019).
[10] L.-F. Lin, Y. Zhang, A. Moreo, E. Dagotto, and S. Dong, Frustrated dipole order induces noncollinear proper ferrielectricity in two dimensions, Phys. Rev. Lett. **123**, 067601 (2019).
[11] L. Li and M. Wu, Binary compound bilayer and multilayer with vertical polarizations: two-dimensional ferroelectrics, multiferroics, and nanogenerators, ACS Nano **11**, 6382 (2017).
[12] M. Wu and J. Li, Sliding ferroelectricity in 2D van der Waals materials: Related physics and future opportunities, Proc. Natl. Acad. Sci. USA **118**, e2115703118 (2021).
[13] Z. Fei, W. Zhao, T. A. Palomaki, B. Sun, M. K. Miller, Z. Zhao, J. Yan, X. Xu, and D. H. Cobden, Ferroelectric switching of a two-dimensional metal, Nature (London) **560**, 336 (2018).
[14] P. Sharma, F.-X. Xiang, D.-F. Shao, D. Zhang, E. Y. Tsymbal, A. R. Hamilton, and J. Seidel, A room-temperature ferroelectric semimetal, Sci. Adv. **5**, eaax5080 (2019).
[15] J. Xiao, Y. Wang, H. Wang, C. D. Pemmaraju, S. Wang, P. Muscher, E. J. Sie, C. M. Nyby, T. P. Devereaux, X. Qian, X. Zhang, and A. M. Lindenberg, Berry curvature memory through electrically driven stacking transitions, Nat. Phys. **16**, 1028 (2020).
[16] K. Yasuda, X. Wang, K. Watanabe, T. Taniguchi, and P. Jarillo-Herrero, Stacking-engineered ferroelectricity in bilayer boron nitride, Science **372**, 1458 (2021).
[17] M. V. Stern, Y. Waschitz, W. Cao, I. Nevo, K. Watanabe, T. Taniguchi, E. Sela, M. Urbakh, O. Hod, and M. B. Shalom, Interfacial ferroelectricity by van der Waals sliding, Science **372**, 1462 (2021).
[18] X. Wang, K. Yasuda, Y. Zhang, S. Liu, K. Watanabe, T. Taniguchi, J. Hone, L. Fu, and P. Jarillo-Herrero, Interfacial ferroelectricity in rhombohedral-stacked bilayer transition metal dichalcogenides, Nat. Nanotechnol. **17**, 367 (2022).
[19] Y. Wan, T. Hu, X. Mao, J. Fu, K. Yuan, Y. Song, X. Gan, X. Xu, M. Xue, X. Cheng, C. Huang, J. Yang, L. Dai, H. Zeng, and E. Kan, Room-temperature ferroelectricity in $1T'$-ReS_2 multilayers, Phys. Rev. Lett. **128**, 067601 (2022).
[20] F. Sui, M. Jin, Y. Zhang, R. Qi, Y.-N. Wu, R. Huang, F. Yue, and J. Chu, Sliding ferroelectricity in van der Waals layered γ-InSe semiconductor, Nat. Commun. **14**, 36 (2023).
[21] L.-P. Miao, N. Ding, N. Wang, C. Shi, H.-Y. Ye, L. Li, Y.-F. Yao, S. Dong, and Y. Zhang, Direct observation of geometric and sliding ferroelectricity in an amphidynamic crystal, Nat. Mater. **21**, 1158 (2022).
[22] X. Liu, A. P. Pyatakov, and W. Ren, Magnetoelectric coupling in multiferroic bilayer VS_2, Phys. Rev. Lett. **125**, 247601 (2020).
[23] T. Zhang, Y. Liang, X. Xu, B. Huang, Y. Dai, and Y. Ma, Ferroelastic-ferroelectric multiferroics in a bilayer lattice, Phys. Rev. B **103**, 165420 (2021).

[24] X. Ma, C. Liu, W. Ren, and S. A. Nikolaev, Tunable vertical ferroelectricity and domain walls by interlayer sliding in β-ZrI_2, npj Comput. Mater. **7**, 177 (2021).

[25] N. Ding, J. Chen, C. Gui, H. You, X. Yao, and S. Dong, Phase competition and negative piezoelectricity in interlayer-sliding ferroelectric ZrI_2, Phys. Rev. Mater. **5**, 084405 (2021).

[26] X. Chen, X. Ding, G. Gou, and X. C. Zeng, Strong sliding ferroelectricity and interlayer sliding controllable spintronic effect in two-dimensional HgI_2 layers, Nano Lett. **24**, 3089 (2024).

[27] P. Meng, Y. Wu, R. Bian, E. Pan, B. Dong, X. Zhao, J. Chen, L. Wu, Y. Sun, Q. Fu, Q. Liu, D. Shi, Q. Zhang, Y.-W. Zhang, Z. Liu, and F. Liu, Sliding induced multiple polarization states in two-dimensional ferroelectrics, Nat. Commun. **13**, 7696 (2022).

[28] K. Liu, X. Ma, S. Xu, Y. Li, and M. Zhao, Tunable sliding ferroelectricity and magnetoelectric coupling in two-dimensional multiferroic MnSe materials, npj Comput. Mater. **9**, 16 (2023).

[29] L. Yang, S. Ding, J. Gao, and M. Wu, Atypical sliding and moiré ferroelectricity in pure multilayer graphene, Phys. Rev. Lett. **131**, 096801 (2023).

[30] Y. Liang, N. Mao, Y. Dai, L. Kou, B. Huang, and Y. Ma, Intertwined ferroelectricity and topological state in two-dimensional multilayer, npj Comput. Mater. **7**, 172 (2021).

[31] R.-C. Xiao, Y. Gao, H. Jiang, W. Gan, C. Zhang, and H. Li, Non-synchronous bulk photovoltaic effect in two-dimensional interlayer-sliding ferroelectrics, npj Comput. Mater. **8**, 138 (2022).

[32] J. Zhou, Photo-magnetization in two-dimensional sliding ferroelectrics, npj 2D Mater. Appl. **6**, 15 (2022).

[33] J. Ji, G. Yu, C. Xu, and H. J. Xiang, General theory for bilayer stacking ferroelectricity, Phys. Rev. Lett. **130**, 146801 (2023).

[34] Z. Hu, M. Tian, B. Nysten, and A. M. Jonas, Regular arrays of highly ordered ferroelectric polymer nanostructures for non-volatile low-voltage memories, Nat. Mater. **8**, 62 (2009).

[35] J.-J. Zhang, J. Guan, S. Dong, and B. I. Yakobson, Room-temperature ferroelectricity in group-IV metal chalcogenide nanowires, J. Am. Chem. Soc. **141**, 15040 (2019).

[36] S. Song, C. Gui, S. Dong, D. Liu, and J. Guan, Adjustable 1D ferroelectricity and ferrielectricity in faceted GeSe nanotubes, J. Mater. Chem. C **12**, 6487 (2024).

[37] C. Yang, M. Chen, S. Li, X. Zhang, C. Hua, H. Bai, C. Xiao, S. A. Yang, P. He, Z.-A. Xu, and Y. Lu, Coexistence of ferroelectricity and ferromagnetism in one-dimensional SbN and BiN nanowires, ACS Appl. Mater. Interfaces **13**, 13517 (2021).

[38] L.-F. Lin, Y. Zhang, A. Moreo, E. Dagotto, and S. Dong, Quasi-one-dimensional ferroelectricity and piezoelectricity in WOX_4 halogens, Phys. Rev. Mater. **3**, 111401(R) (2019).

[39] W. Sun, N. Ding, J. Chen, H.-P. You, J. Peng, S.-S. Wang, and S. Dong, Stacking dependent ferroelectricity and antiferroelectricity in quasi-one-dimensional oxyhalides $NbOX_3$, Phys. Rev. Mater. **6**, 104404 (2022).

[40] L. Zhang, C. Tang, S. Sanvito, and A. Du, Purely one-dimensional ferroelectricity and antiferroelectricity from van der Waals niobium oxide trihalides, npj Comput. Mater. **7**, 135 (2021).

[41] R. He, B. Zhang, H. Wang, L. Li, P. Tang, G. Bauer, and Z. Zhong, Ultrafast switching dynamics of the ferroelectric order in stacking-engineered ferroelectrics, Acta Mater. **262**, 119416 (2024).

[42] G. Kresse and J. Furthmüller, Efficient iterative schemes for *ab initio* total-energy calculations using a plane-wave basis set, Phys. Rev. B **54**, 11169 (1996).

[43] J. P. Perdew, K. Burke, and M. Ernzerhof, Generalized gradient approximation made simple, Phys. Rev. Lett. **77**, 3865 (1996).

[44] S. Grimme, Semiempirical GGA-type density functional constructed with a long-range dispersion correction, J. Comput. Chem. **27**, 1787 (2006).

[45] S. Grimme, J. Antony, S. Ehrlich, and H. Krieg, A consistent and accurate *ab initio* parametrization of density functional dispersion correction (DFT-D) for the 94 elements H-Pu, J. Chem. Phys. **132**, 154104 (2010).

[46] Y. L. Page and P. Saxe, Symmetry-general least-squares extraction of elastic data for strained materials from *ab initio* calculations of stress, Phys. Rev. B **65**, 104104 (2002).

[47] X. Wu, D. Vanderbilt, and D. R. Hamann, Systematic treatment of displacements, strains, and electric fields in density-functional perturbation theory, Phys. Rev. B **72**, 035105 (2005).

[48] R. D. King-Smith and D. Vanderbilt, Theory of polarization of crystalline solids, Phys. Rev. B **47**, 1651 (1993).

[49] R. Resta, Macroscopic polarization in crystalline dielectrics: The geometric phase approach, Rev. Mod. Phys. **66**, 899 (1994).

[50] S. L. Dudarev, G. A. Botton, S. Y. Savrasov, C. J. Humphreys, and A. P. Sutton, Electron-energy-loss spectra and the structural stability of nickel oxide: An LSDA + U study, Phys. Rev. B **57**, 1505 (1998).

[51] M. Cococcioni and S. de Gironcoli, Linear response approach to the calculation of the effective interaction parameters in the LDA + U method, Phys. Rev. B **71**, 035105 (2005).

[52] See Supplemental Material at http://link.aps.org/supplemental/10.1103/PhysRevB.110.024115 for more details about the possible magnetic orders and the phonon spectrum of the nonpolar antiferromagnetic state.

[53] L. Dahl and D. Wampler, The crystal structure of α-niobium tetraiodide, Acta Crystallogr. **15**, 903 (1962).

[54] Z. Wang and S. Dong, Alterferroicity with seesaw-type magnetoelectricity, Proc. Natl. Acad. Sci. USA **120**, e2305197120 (2023).

[55] Q. Yang, M. Wu, and J. Li, Origin of two-dimensional vertical ferroelectricity in WTe_2 bilayer and multilayer, J. Phys. Chem. Lett. **9**, 7160 (2018).

[56] X. Liu, Y. Yang, T. Hu, G. Zhao, C. Chen, and W. Ren, Vertical ferroelectric switching by in-plane sliding of two-dimensional bilayer WTe_2, Nanoscale **11**, 18575 (2019).

[57] L. You, Y. Zhang, S. Zhou, A. Chaturvedi, S. A. Morris, F. Liu, L. Chang, D. Ichinose, H. Funakubo, W. Hu, T. Wu, Z. Liu, S. Dong, and J. Wang, Origin of giant negative piezoelectricity in a layered van der Waals ferroelectric, Sci. Adv. **5**, eaav3780 (2019).

[58] Y. Qi and A. M. Rappe, Widespread negative longitudinal piezoelectric responses in ferroelectric crystals with layered structures, Phys. Rev. Lett. **126**, 217601 (2021).

[59] V. Wang, N. Xu, J.-C. Liu, G. Tang, and W.-T. Geng, VASPKIT: A user-friendly interface facilitating high-throughput computing and analysis using VASP code, Comput. Phys. Commun. **267**, 108033 (2021).

[60] X. Gonze and C. Lee, Dynamical matrices, born effective charges, dielectric permittivity tensors, and interatomic force

constants from density-functional perturbation theory, Phys. Rev. B **55**, 10355 (1997).

[61] F. Mouhat and F.-X. Coudert, Necessary and sufficient elastic stability conditions in various crystal systems, Phys. Rev. B **90**, 224104 (2014).

[62] M. de Jong, W. Chen, H. Geerlings, M. Asta, and K. A. Persson, A database to enable discovery and design of piezoelectric materials, Sci. Data **2**, 150053 (2015).

[63] M. Imada, A. Fujimori, and Y. Tokura, Metal-insulator transitions, Rev. Mod. Phys. **70**, 1039 (1998).